Lawrence Berkeley National Laboratory
Energy Geosciences

Title
Continuum Modelling of Cyclic Steam Injection in Diatomite

Permalink
https://escholarship.org/uc/item/4gq8q5tr

ISBN
9781613998557

Authors
Smith, J Torquil
Sonnenthal, Eric L
Milliken, William J

Publication Date
2022-04-19

DOI
10.2118/209331-ms

Copyright Information

Peer reviewed

Please fill in your author name(s) and company affiliation.

Given Name	Middle Name	Surname	Company
J	Torquil	Smith	Lawrence Berkeley National Laboratory
Eric	L	Sonnenthal	Lawrence Berkeley National Laboratory
William	J	Milliken	Chevron Corporation

Abstract

Objectives/Scope: Steam injection in diatomite reservoirs results in permeability changes owing to fracture propagation, and compaction as a result of thermal effects and pressure changes during injection and production. The purpose of this work is to evaluate these coupled thermal, hydrological, and mechanical (THM) processes over several years of cyclic steam injection and production. A single well model in a diatomite reservoir was created to evaluate processes at a higher resolution near well-bore than used in a 3-D reservoir-scale model.

Methods, Procedures, Process: Simulations include tensile failure, shear failure with simultaneous shear on multiple planes, coupling of porosity and permeability changes with multiphase flow, and diatomite compaction with temperature and effective stress. Initial isotropic horizontal stresses are 1.0375 of vertical (azimuthal average, part of San Joaquin Valley). Injection interval (437-528 m) pressure is fixed, 6.3 MPa, 930 psi (injection), and ~4 MPa (production), with a soak between. Three degree dilation on shearing is assumed. To the extent that fracture opening is tensile, fractures close on fluid pressure drop, but shear components remain. Permeability changes due to mechanical failure are simulated using a cubic law.

Results, Observations, Conclusions: During injection over multiple cycles, the diatomite surrounding the well is heated to over 250 °C and pressurized by the injected steam. During soak (shut-in) and subsequent production, pressure drops, dropping the boiling point, inducing further vaporization. Geomechanical changes show tensile opening accompanied by a greater amount of shearing. Total shearing increases with each injection cycle, resulting in a greater porosity increase from shearing than tensile opening. Fracture propagation was limited to the diatomite reservoir and did not penetrate the caprock.

Novel/Additive Information: Inclusion of an empirical effective stress/temperature diatomite compaction law together with porosity and permeability changes due to mechanical failure more closely models the mechanics of cyclic steaming of diatomite.

# Continuum Modelling of Cyclic Steam Injection in Diatomite

Steam injection in diatomite reservoirs results in permeability changes owing to fracture propagation, and compaction as a result of thermal effects and pressure changes during injection and production. We model a single well model in a diatomite reservoir, using the continuum thermal-hydrological-mechanical-chemical modelling code TReactMech (Kim et al., 2012, Smith et al., 2015) based on TOUGHREACT V3.32-OMP (Sonnenthal and Spycher, 2017). The code uses sequential coupling of multi-phase hydrological flow and mechanics; on each time step flow equations are solved for pressure, temperature (or gas saturation) and porosity determined from pressure, temperature, and volumetric stress, and mechanics equations solved for nodal displacements, and stress and strain determined from nodal displacements (Kim, et al. 2012, Smith, et al. 2017). Within the formation and solution of mechanics equations, Mohr-Coulomb failure and tensile failure criteria are computed, and material failure allowed, with possibly multiple simultaneous modes of failure in a grid block solved for using the return mapping algorithm (e.g., Borja, et al. 2003). Changes in permeability due to poro-elastic changes in porosity and due to changes in porosity due to material failure are modelled using cubic laws. Inelastic diatomite compaction with effective stress and temperature is parametrized as bilinear in effective stress σ_{eff} and offset temperature $T - T_{bi0}$;

$$\epsilon_{dis} = \sigma_{eff} \cdot \left[(T - T_{bi0}) c_{bi} - \frac{1}{3 K_{bulk}} \right] - \epsilon_{dis0} , \tag{1a}$$

where ϵ_{dis} is inelastic compaction strain, c_{bi} and T_{bi0} are parameters, K_{bulk} is bulk modulus,

$$\epsilon_{dis0} = \sigma_{eff0} \cdot \left[(T_{t=0} - T_{bi0}) c_{bi} - \frac{1}{3 K_{bulk}} \right] , \tag{1b}$$

and σ_{eff0} is initial effective stress. (Quantities T, σ_{eff}, σ_{eff0}, ϵ_{dis}, ϵ_{dis0} generally vary with position). Letting $\overline{\sigma}_{eff} \equiv trace(\sigma_{eff})/3$ be the volumetric effective stress, Eqs. (1a-b) are used for volumetric effective stress temperature product $\overline{\sigma}_{eff} \cdot (T - T_{bi0})$ magnitude increasing above its previous maximum magnitude at a point. Between T_1=160 and T_2=200 $^\circ$C variation with temperature is rolled off as a quadratic in T to flatten with respect to T at T_2, and variation with temperature is neglected above T_2. Parameters c_{bi} and T_{bi0} were fitted to diatomite compaction data from Dietrich and Scott (2007); liquid water saturated diatomite compaction data with temperature to 168 $^\circ$C and effective stress to 10.1 MPa, and water vapor saturated diatomite data with temperature to 102 $^\circ$C, giving c_{bi} =1.63x10^{-10} / $^\circ$C-Pa and T_{bi0}= -47.9 $^\circ$C. Data for vapor saturated diatomite above 102 $^\circ$C was not used, as it is presumed to be at pressures well below vapor saturation pressure. Compaction strain is plotted in **Fig. 1** for volumetric effective stress temperature product magnitude increasing above it previous (local) maximum; for this plot, the 1/3 K_{bulk} term has been omitted, so that strains have their approximate values with elastic strain included. For volumetric effective stress temperature product $\overline{\sigma}_{eff} \cdot (T - T_{bi0})$ magnitude below its previous maximum magnitude at a point (e.g., decreasing), the changes in inelastic strain implied by changing T and σ_{eff} in Eq. (1a), are reduced by a factor b_{bi}. In the current work b_{bi} =0, so there is only ordinary elastic and thermal contraction when $\overline{\sigma}_{eff} \cdot (T - T_{bi0})$ is decreasing.
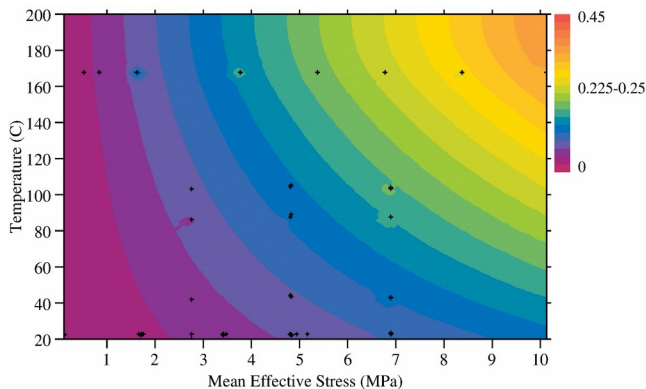
Fig. 1. Fitted bilinear temperature-effective stress strain for 20 ≤ *T* ≤ 160 °C, with quadratic extension for 160 ≤*T* ≤ 200 °C, for volumetric effective stress shifted temperature product $\overline{\sigma}_{eff} \cdot (T - T_{bi0})$ increasing. Dietrich and Scott (2007) data shown (inserted) at crosses.

The simulation was made on a 21x21x121 grid with 5 m horizontal spacing at its center, expanding outwards to ±197.5 m, and with 9.1 m vertical spacing at its center, expanding to extend from -2465 to 299 m vertically. No fluid flow, no heat flow, and no normal mechanical displacement boundary conditions were used at edges in x and y, simulating periodic continuation with 395 m periodicity. Initial horizontal stresses were assumed to be 1.0375 times vertical loading stresses, a ratio consistent with azimuthally averaged horizontal stress near the San Andreas fault by the southwest edge of the San Joaquin Valley, Calif. (Mount and Suppe, 1987). Properties directly affecting flow are given in **Table 1**. Horizontal permeability is shown in cross section in **Fig. 2**. Mechanical properties are given in **Table 2**. between The target reservoir is in opal-A diatomite from *z*=-348 to -92 m, with more compact opal CT diatomite below it, and various sediments, including reworked diatomite above it. Young's modulus and shear modulus in the diatomite are an average of three values measured for 'clean' Belridge diatomite (Fossum and Friedrich, 2000).
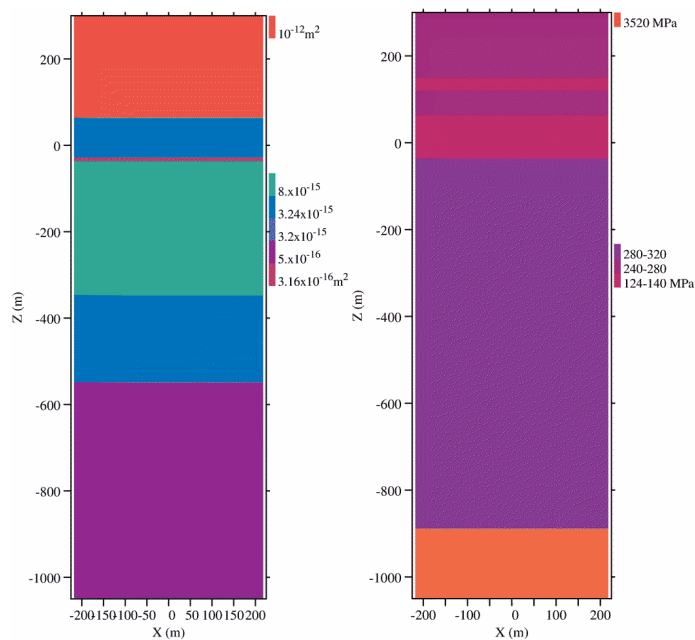

**Fig. 2. (Left) horizontal permeability, (right) Young's modulus, cross section, central part.**

For the simulation, a well was assumed perforated over 91 m, with a 150 ft (45.7 m) stand-off from the top of the diatomite, that is, it is perforated from *z*=-229 to -138 m. Injection and production were simulated by holding well cells to fixed pressures during injection and production. Down-hole injection pressure was 6.3 MPa (930 psi). Injection vapor saturation was fixed to correspond to 70 % steam quality (vapor mass portion). Down-hole production pressures were assumed to be 689 kPa (100 psi) plus 7.83 kPa/m head, the head corresponding to liquid water density at 250 °C. The production schedule was approximated by 18 cycles per year, with two days injection, 0.5 days soak (shut-in), and 17.8 days production, each cycle. During production, well temperature was constrained to follow the temperature of adjacent rock. In these simulations, only water was considered for the liquid phase, neglecting the oil component.

Temperature peaks simultaneously with pressure, and vapor saturation peaks slightly after the end of each injection phase (**Fig. 3**). Mixed phase conditions persist a bit longer on each cycle, before reverting

to liquid phase, and after 2070 days (202 cycles), remains mixed phase. Total injection and total production over all well cells are plotted in **Fig. 4**. The ratio of production to injection (1.0) is lower than the ratio (1.2) observed for wells the modelled geology is based on, indicating that the simulation assumed down-hole production pressures are too high, and need to be reduced to match the actual ratio. Volumetric stress peaks coincide closely with peaks in fluid pressure (**Fig. 5**, left). Volumetric strain peaks similarly coincide with peaks in volumetric stress, with a long term net compaction due to effective stress temperature product strain (**Fig. 5**, right).
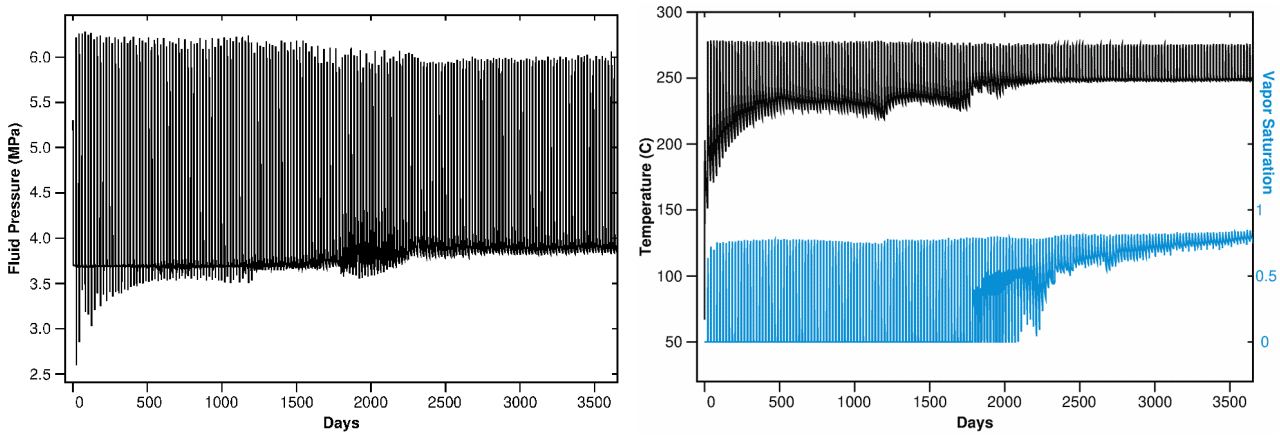
Fig. 3. (Left) fluid pressure, (right) temperature and vapor saturation, in uppermost cell penetrated by perforated well.
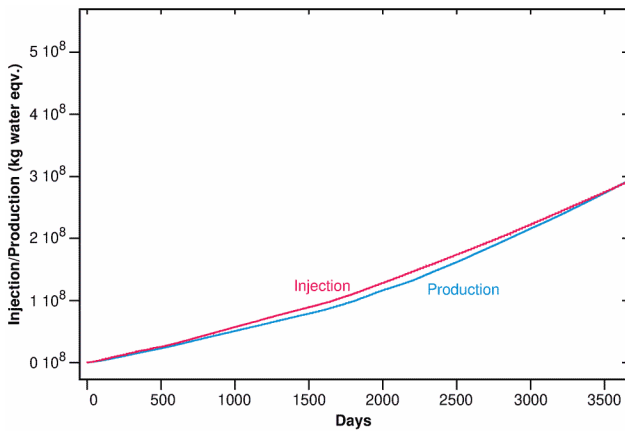

Fig. 4. Total injection and total production, in kg water equivalent volume.
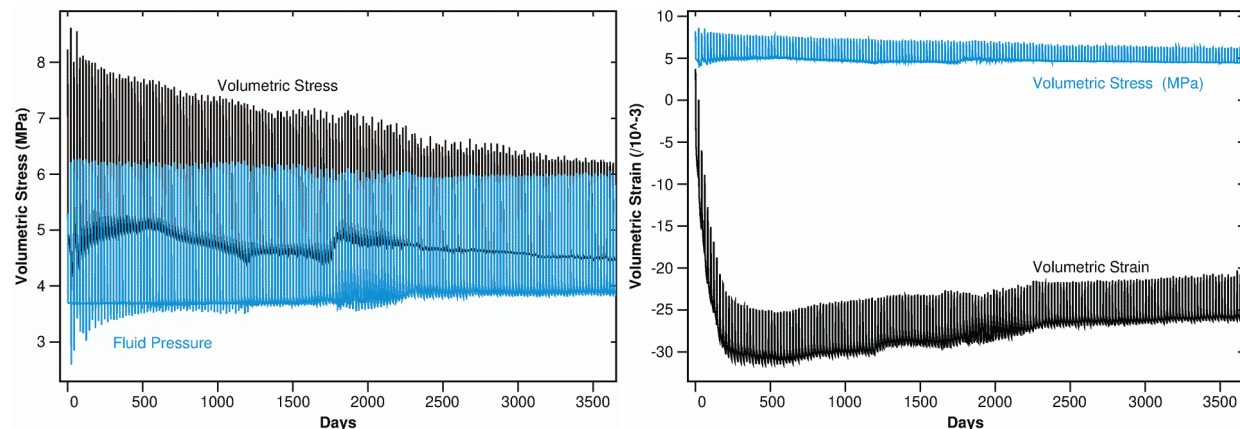
Fig. 5. (Left) volumetric stress (black, envelope discernable), and fluid pressure (blue), (right) volumetric strain and stress, in uppermost cell penetrated by perforated well.

The total volume of induced cracks increases in time, with sharp peaks roughly coincident with peaks in fluid pressure (**Fig. 6**). The increasing crack opening yields increased permeability, and increased flow with time (**Fig. 4**). On all but the first two injection cycles, cracks open in a triple failure mode in the vicinity of the well; shear failure on two independent planes and tensile failure in a third, resulting in significant crack volume.
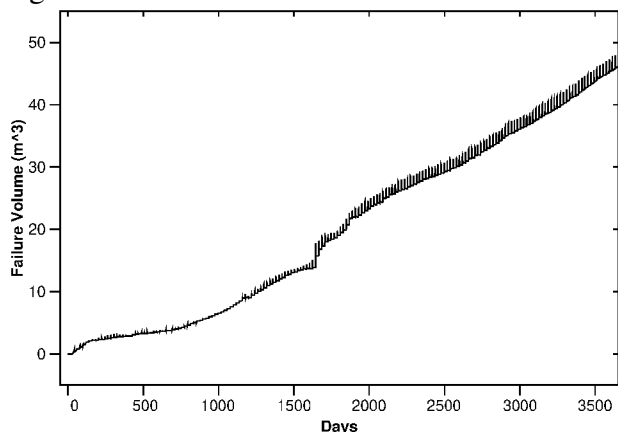

Fig. 6. Total volume of induced cracks.

Rock around the well heats up, reaching a temperature (255 °C) intermediate between vapor saturation temperatures at injection and production pressures (**Fig. 7**, left). It progressively compacts from effective stress temperature product strain, attaining compaction of up to 4.2 % after 171 cycles (**Fig. 7**, right). Rock failure occurs in the vicinity of the perforated well (**Fig. 8**, left). Integrating the failure (crack) porosity with respect to y coordinate gives the integrated aperture (**Fig. 8**, middle, at end of an injection). During the soak and production periods, pressure in the rock about the well drops, and tensile cracks close up, leaving crack volume due to dilation due to movement on shear failure surfaces (**Fig. 8**, right) (a 3° dilation angle is assumed).
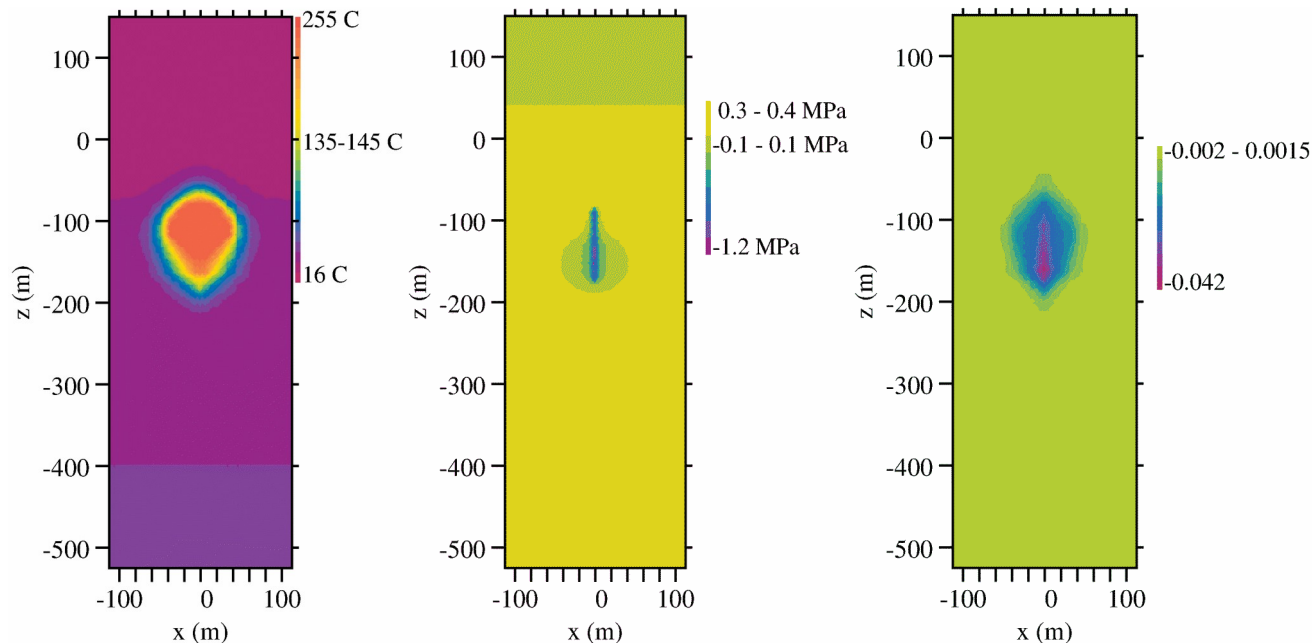
Fig. 7. (Left) temperature, (middle) fluid pressure change, (right) volumetric strain, vertical cross section through well, details, at end of 171'st production phase (day 3470).
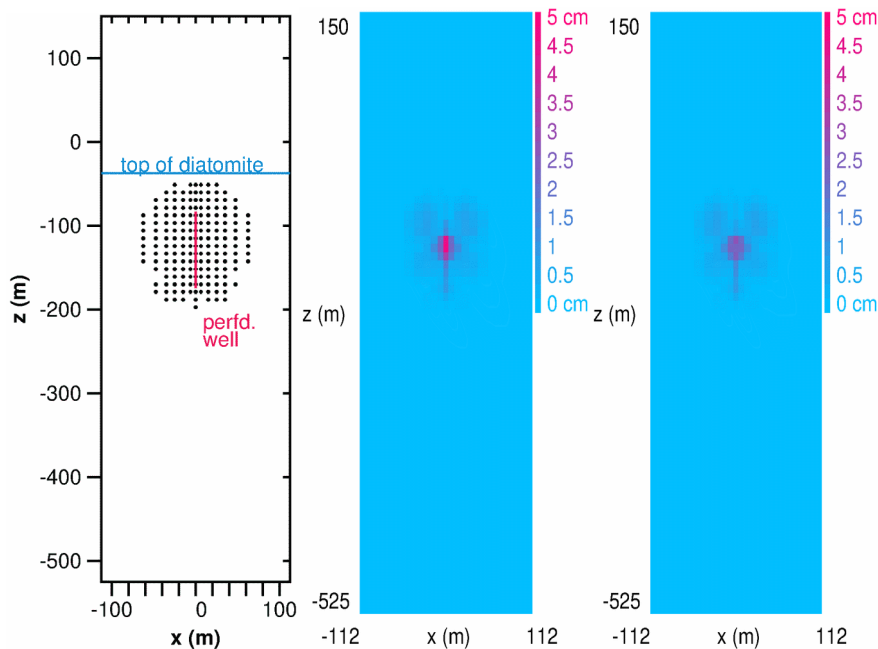
Fig. 8. (Left) location of rock failure, projected on vertical plane, detail, (middle) integrated aperture on vertical plane, detail, at end of
188'th injection (day 3635). (Right) integrated aperture on vertical plane, detail, at end of 188'th production phase (day 3652).

There is 0.43 m net upwards displacement at the surface (z=299 m) after 3470 days, whereas actual production is believed to have resulted in net subsidence. The discrepancy is probably a result of the too high assumed down-hole production pressure and too low production/injection ratio previously discussed. This leads to slight long term pressure increases away from the well (**Fig. 7**, middle), and poroelastic dilation, integrating to net uplift.

Conclusion

During injection over multiple cycles, the diatomite surrounding the well is heated to over 250 ˚C and pressurized by the injected steam. During soak and subsequent production, pressure drops, dropping the boiling point, inducing further vaporization. Geomechanical changes show tensile opening accompanied by a greater amount of shearing. Total shearing increases with each injection cycle, resulting in a greater porosity increase from shearing than tensile opening. Fracture propagation did not extend through the top of the diatomite and the maximum horizontal extent was about 80 meters from the well. Inclusion of an empirical effective stress/temperature diatomite compaction law together with porosity and permeability changes due to mechanical failure more closely models the mechanics of cyclic steaming of diatomite.

Vertical Range (m)	Porosity	Permeability kx & ky, kz (m^2)	Thermal Conduct. (wet, dry) (W/m K)	Grain Heat Capacity (J/kg)	Grain Density (kg/m^3)
264-299	0.4000	1.0x10^{-12}	1.20, 0.90	724.	1500.
149-264	0.3600	1.0x10^{-12}	1.80, 1.35	724.	2500.

120-149	0.3600	1.0x10^{-12}, 1.0x10^{-14}	1.80, 1.35	724.	2500.
63-120	0.3714	1.0x10^{-12}, 1.0x10^{-14}	1.80, 1.35	724.	2500.
8-63	0.5876	3.2x10^{-15}, 3.2x10^{-16}	1.50, 1.125	724.	2400.
-37-8	0.5876	3.6x10^{-16}	1.50, 1.125	724.	2400.
-92 - -37	0.6600	8.2x10^{-15}, 4.1x10^{-15}	1.20, 0.90	724.	2300.
-211 - -92	0.6500	8.2x10^{-15}, 4.1x10^{-15}	1.20, 0.90	724.	2300.
-348 - -211	0.6000	8.0x10^{-15}, 4.0x10^{-15}	1.30, 0.975	724.	2300.
-549 - -348	0.5900	3.24x10^{-15}	1.30, 0.975	724.	2350.
-890 - -549	0.4500	5.0x10^{-16}	1.30, 0.975	800.	2400.
-2465 - -890	0.3500	1.0x10^{-15}	1.40, 1.05	884.	2350.

Table 1. Model flow parameters.

Vertical Range (m)	Youngs Mod. (GPa)	Shear Mod. (GPa)	Poisson Ratio	Friction Angle (deg)	Cohesion (MPa)	Tensile strength (MPa)	Dilation Angle (deg)	Biot Coef.	Therm.Expan. Coef (°C-1)
264-299	0.2806	0.1039	0.35	25.6	1500.	1000.	2.0	0.99601	4.45x10^{-5}
149-264	0.2806	0.1039	0.35	37.	1.0	1.0	2.0	0.99601	4.45x10^{-5}
120-149	0.1391	0.04825	0.4414	35.	1.0	1.0	2.0	0.99601	4.45x10^{-5}
63-120	0.2408	0.09074	0.3267	25.6	1.0	1.0	2.0-3.0	0.99369	3.0x10^{-5}
8-63	0.1244	0.04332	0.3267	25.6	1.0	1.0	3.0	0.99258	4.45x10^{-5}
-37-8	0.1244	0.04332	0.4479	25.6	1.0	1.0	3.0	0.99258	4.45x10^{-5}
-93 – -37	0.4892	0.2020	0.2109	25.6	0.0	0.0	3.0	0.99232	4.45x10^{-5}
-211 – -92	0.4892	0.2020	0.2109	25.6	0.0	0.0	3.0	0.99232	4.45x10^{-5}
-348 – -211	0.4892	0.2020	0.2109	25.6	0.0	0.0	3.0	0.99232	4.45x10^{-5}
-549 – -348	0.4892	0.2020	0.2109	25.6	1.0	1.0	2.0	0.99232	4.45x10^{-5}
-890 – -549	0.4892	0.2020	0.2109	25.6	1.0	1.0	2.0	0.99232	4.45x10^{-5}
-2465 – -890	3.5217	1.5110	0.1654	25.6	1.0	1.0	3.0	0.95221	4.45x10^{-5}

Table 2. Mechanical parameters.

References

Borja, R.I., Samma, K.M., and Sanz, P.F., 2003. On the numerical integration of three-invariant elastoplastic constitutive models. *Comput. Methods Appl. Mech. Engrg*. 192, 1227-1258.

Dietrich, J.K., Scott, J.D., 2007. Modeling thermally induced compaction in diatomite. *SPE Journal*, March 2007, SPE 97849, 130-144.

Fossum and Fredrich, 2000, Constitutive models for Etchegoin sands, Belridge diatomite, and overburden formations, at the Lost Hills oil field, California. Technical report SAND2000-0827, Sandia National Laboratories, Albuquerque, New Mexico.

Kim, J., Sonnenthal, E.L., and Rutqvist, J., 2012. Formulation and sequential numerical algorithms of coupled fluid/heat flow and geomechanics for multiple porosity materials, *Int. J. Numer. Meth. Engng.*, 92, 425-456.

Mount, V.S., Suppe, J., 1987. State of stress near the San Andreas fault: implications for wrench tectonics. *Geology*, 15, 1143-1146.

Smith, J.T., Sonnenthal, E.L., and Cladouhos, T., 2015. Thermal-Hydrological-Mechanical Modelling of Shear Stimulation at Newberry Volcano, Oregon. *Proceedings of 49th US Rock Mechanics/Geomechanics Symposium*, American Rock Mechanics Association, ARMA 15-0680.

Sonnenthal, E.L., Spycher, N., 2017. TOUGHREACT V3.32-OMP, https://tough.lbl.gov/software/ toughreact.